



Grain coarsening on the free surface and in the thickness direction of a sphere-forming triblock copolymer film

Rasha Ahmed Hanafy Bayomi^{1,2} · Konomi Honda¹ · Isao Wataoka¹ · Hideaki Takagi³ · Nobutaka Shimizu³ · Noriyuki Igarashi³ · Sono Sasaki¹ · Shinichi Sakurai^{1,4}

Received: 6 April 2018 / Revised: 18 May 2018 / Accepted: 22 May 2018 / Published online: 6 July 2018
© The Society of Polymer Science, Japan 2018

Abstract

Controlling a block copolymer “grain”, in which the microdomains are regularly ordered in a single lattice, is important for developing high-performance polymeric materials. This is because the grains, which are several micrometers in size, can directly affect the properties of the materials. In this regard, we focused on grain coarsening on the free surface and in the thickness direction of a sphere-forming triblock copolymer film. We evaluated the grain size on the free surface using atomic force microscopy combined with image processing, and in the thickness direction, we used small-angle X-ray scattering edge-view measurements. It was found that the grain growth in the direction parallel to the free surface was very slow in the early stage of thermal annealing. Then, the grain growth shifted to a rapid growth mechanism with a power-law relationship (grain size $\sim t^\alpha$, with $\alpha = 0.7$) after ~ 30 min. Based on the value of the growth exponent α , the grain growth mechanism is considered to fall between the random and deterministic processes. In contrast, for the thickness direction, a much larger value ($\alpha = 1.72$) was obtained. For such a large α value, it is impossible to consider the growth mechanism of the grain within the conventional framework of the growth of domains and droplets. Therefore, our results may require a new framework to explain the behavior of the grain growth in the spherical microdomain system. Another notable finding is that the thickness of the oriented layer near the free surface or near the surface in contact with the substrate can be as thick as $9.5 \mu\text{m}$, which is substantially larger than the reported values of the propagation distance of surface-induced orientation of microdomains in block copolymers. Based on the results of the current study, it is speculated that grain growth serves as a propagator for the regular ordering of spherical microdomains and the orientation of the lattice.

Introduction

Revealing structure–property relationships has been a key issue for the development of novel functional or high-performance polymeric materials. In particular, for block copolymers, orienting microdomains has been extensively studied to generate block copolymers with novel material properties [1]. However, less attention has been paid to “grains”, which are a higher rank in the hierarchical structures of block copolymers and are defined as regions

containing microdomains regularly ordered in a single lattice [2]. Because grains are several micrometers in size, the grains may directly affect the properties of these materials. Therefore, controlling the grains is important for controlling the properties of block copolymer materials. Although the application of an external field (shear flow, electric, or magnetic field) [1] can effectively orient a lattice (or microdomain), macroscopic specimens will still be in a polygrain state. In other words, the specimen will comprise many tiny grains with different lattice orientations even

✉ Shinichi Sakurai
shin@kit.ac.jp

¹ Department of Biobased Materials Science, Graduate School of Science and Technology, Kyoto Institute of Technology, Matsugasaki, Kyoto, Sakyo-ku 606-8585, Japan

² Department of Apparel Design and Technology, Faculty of

Applied Arts, Helwan University, Orman, Giza 12111, Egypt

³ Photon Factory, High Energy Accelerator Research Organization, Tsukuba, Ibaraki 305-0801, Japan

⁴ Institute for Chemical Research, Kyoto University, Gokasho, Uji, Kyoto 611-0011, Japan

though the orientation of the microdomains or the orientation of one preferential direction of the lattice is the same in all of the grains (see for example Fig. 1 of ref. 3). To increase the size of the grains, thermal annealing is required [3]. Therefore, in the current paper, we focus on the growth of grains in which spherical microdomains are regularly ordered in a body-centered cubic (bcc) lattice as a function of thermal annealing.

Many studies have reported that grain growth follows a power law with time, as described by the following [3–10]:

$$\xi \sim t^\alpha \quad (1)$$

where ξ is the orientational correlation length (in some studies, it is referred to as the grain size), t is the thermal annealing time, and α is the growth exponent. Harrison et al. [4] examined a monolayer (its thickness allows the existence of only one layer of a plane on which block copolymer microdomains are regularly ordered) of cylinders oriented parallel to the surface of the substrate, and $\alpha = 0.25$ has been reported. A similar value ($\alpha = 0.28$) has been reported by Ji et al. [5] and Black et al. [6] for cylinders oriented perpendicular to the substrate in a thin film with a thickness ranging from 32 to 640 nm. On the other hand, for much thicker film specimens (thicknesses ranging from 45 to 175 μm), Sakurai et al. [3] reported $\alpha = 0.45$ for perpendicularly oriented cylinders. The difference in these values for the perpendicularly oriented cylinders might be due to the extent of the cylinder orientation. Namely, in the former case [5], the perpendicular orientation of the cylinders is limited only to the vicinity of the free surface, while in the latter case, the perpendicular orientation is observed throughout the film specimen. For the perpendicularly oriented lamellae, Hu et al. [7] reported a very small value ($\alpha = 0.07$) for diblock copolymer lamellae and $\alpha = 0.13$ for star block copolymer lamellae. Regarding a spherical microdomain system, Harrison et al. [8] reported $\alpha = 0.25$ as revealed experimentally using a monolayer film of spheres ordered in a hexagonal lattice, and this value was found by simulation studies ($\alpha = 0.20 - 0.25$) [9]. In contrast, Honda et al. [10] reported $\alpha = 1.5$ for film specimens with thicknesses ranging from 5 to 55 μm in which the spheres are ordered in a bcc lattice instead of a hexagonal lattice. Since these α values are substantially different from each other, the thickness of the specimen seems to significantly affect the results. Therefore, we revisit this problem by conducting careful experiments. In the current study, the α value is reexamined for spherical microdomains ordered in a bcc lattice with a film thickness of 43 μm . Notably, based on the experimental results from atomic force microscopy (AFM), we discuss the grain growth on the free surface of the film specimen where the (110) planes of the bcc lattice are spontaneously oriented parallel to the film surface. Furthermore, we separately

discuss the grain coarsening mechanism in the thickness direction based on the small-angle X-ray scattering (SAXS) results.

Experimental

The material used in this study is a polystyrene-*block*-poly(ethylene-*co*-butylene)-*block*-polystyrene triblock copolymer with the code name SEBS-8, which is the same material used in a previous study [10]. It forms polystyrene (PS) spherical microdomains embedded in a matrix of poly(ethylene-*co*-butylene) (PEB). For this sample, $M_n = 6.7 \times 10^4$, the polydispersity index (M_w/M_n) = 1.04, and the volume fraction of PS (ϕ_{PS}) = 0.084, where M_n and M_w denote the number- and weight-average molecular weights, respectively.

For the AFM observations and the grazing incidence small-angle X-ray scattering (GISAXS) measurements, the sample was spin-coated on a silicon wafer ($525 \pm 25 \mu\text{m}$ thick, Yamanaka Hutech Co, Japan) with 2000 rpm for 30 s at room temperature from a toluene solution containing 10 wt% polymer (the specimen thickness was 1.4 μm). Then, the as-spin-coat film was further subjected to the thermal annealing at 140 $^\circ\text{C}$ under a nitrogen atmosphere. Since the order-disorder transition temperature (T_{ODT}) is reported to be 150 $^\circ\text{C}$ for SEBS-8 [11], this annealing temperature was 10 $^\circ\text{C}$ lower than the T_{ODT} , which is appropriate to induce ordering of the PS spherical microdomains in a bcc lattice within several hours. Moreover, the sample was cast on a polyimide (Kapton) film with a 25 μm thickness (DuPont-Toray Co. Ltd., Japan) from a toluene solution containing 10 wt% polymer at room temperature (the specimen thickness was $43.3 \pm 2.2 \mu\text{m}$) for the time-resolved two-dimensional small-angle X-ray scattering (2d-SAXS) measurements.

The surface structures of the specimens were analyzed by AFM in tapping mode by using a SPM9700 instrument (Shimadzu) with a standard scanner (ASSY STD, Shimadzu). The maximum scanning area was $30 \times 30 \mu\text{m}^2$. The used cantilever (NANOSENSORS) had a length of $225 \pm 10 \mu\text{m}$ and a force constant of 5–37 N/m.

The GISAXS measurements were conducted at the BL-6A beamline in Photon Factory, High Energy Accelerator Research Organization, Tsukuba, Japan [12], using the X-ray beam with a wavelength of $\lambda = 0.150 \text{ nm}$. The sample-to-detector distance was 1048.3 mm, and the beam size measured at the detector position was 0.245 mm (an FWHM value) in the vertical direction and 0.498 mm (an FWHM value) in the horizontal direction. A PILATUS3-1M (DECTRIS Ltd., Baden, Switzerland) was used as a two-dimensional detector. The incident angle ranged from 0.12° to 0.13° . Note here that the scattering depth [13, 14]

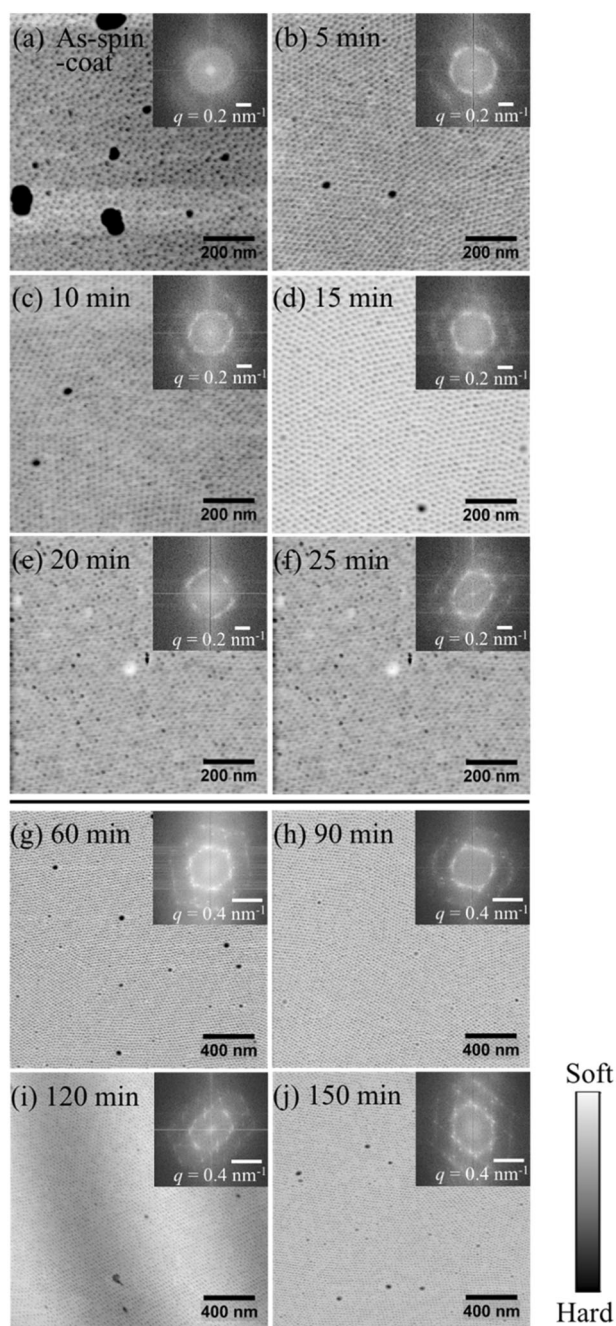


Fig. 1 AFM phase images of the SEBS-8 specimens as a function of thermal annealing time; (a) as-spin-coat specimen, (b) 5, (c) 10, (d) 15, (e) 20, (f) 25, (g) 60, (h) 90, (i) 120, and (j) 150 min annealed specimens

for the experimental conditions of the GISAXS measurements were calculated to be 19.4–22.5 nm at the so-called Yoneda wing. Considering that the spacing of the {110} planes of the bcc lattice in SEBS-8, measured by SAXS (the data are shown in Fig. 7b), is $d_{110} = 22.9$ nm, the conditions of the GISAXS measurements with $\alpha_i = 0.12^\circ$ – 0.13° corresponds to probing the ordering of the PS spherical

microdomains that are present only in the outermost monolayer of the specimen.

The 2d-SAXS edge-view measurements (see the schematic illustration in Fig. 7b) were performed using a Nano-Viewer (MicroMax-007HF) apparatus (Rigaku Co., Ltd., Akishima, Tokyo, Japan) composed of a rotating-anode X-ray generator with an electron gun consisting of a tungsten filament, an Osmotic Confocal Max Flux Mirror (CMF, Rigaku Co., Ltd.) for focusing the X-ray beam, and three collimation pinhole slits (0.3, 0.25, and 0.3 mm ϕ for the first, second, and third slits, respectively) [15]. The wavelength components other than CuK α ($\lambda = 0.154$ nm) were eliminated using a Ni filter. The sample-to-detector distance was set to 1 m. The focal length of the CMF mirror was 900 mm, and the distance from the mirror to the 2d-detector (PILATUS 100 K, DECTRIS Ltd., Baden, Switzerland) was 2000 mm in the Rigaku Nano-Viewer SAXS collimation; therefore, the X-ray beam on the 2d-detector was defocused, causing the measured 2d-SAXS patterns to be smeared. However, the extent of smearing was considered to be trivial such that desmearing of the measured 2d-SAXS patterns were not conducted. To determine the mechanism of the grain growth in the thickness direction, we conducted time-resolved 2d-SAXS edge-view measurements as a function of thermal annealing. The 2d-SAXS measurements were conducted at room temperature using a single specimen as a function of annealing time (the annealing temperature was 140 °C). Namely, once the SAXS measurements were completed for the as-cast specimen, this specimen was thermally annealed for 28 min in an N₂-purged oven. After quenching to room temperature, this annealed specimen was again subjected to 2d-SAXS measurements with the same position of the specimen being illuminated by the incident X-ray beam. This procedure was repeated many times to measure the 2d-SAXS patterns as a function of annealing time.

Results and discussion

Figure 1 shows the AFM phase images of the SEBS-8 specimens as a function of thermal annealing time at 140 °C. Note that the magnification for the images shown in Fig. 1g–j is lower than that of the images in Fig. 1a–f. To quantitatively discuss the improvement in the regularity, we conducted Fourier transform (FT) analyses by using ImageJ (free software [16]), which are shown as insets. Here, q denotes the magnitude of the wavenumber, as defined by $q = 2\pi/d$ with d being the line spacing. The bright and dark browns correspond to the soft and hard regions, respectively. Therefore, the small, dark brown domains are considered to be the PS spherical microdomains. As a result of quick solvent evaporation during spin coating, a random

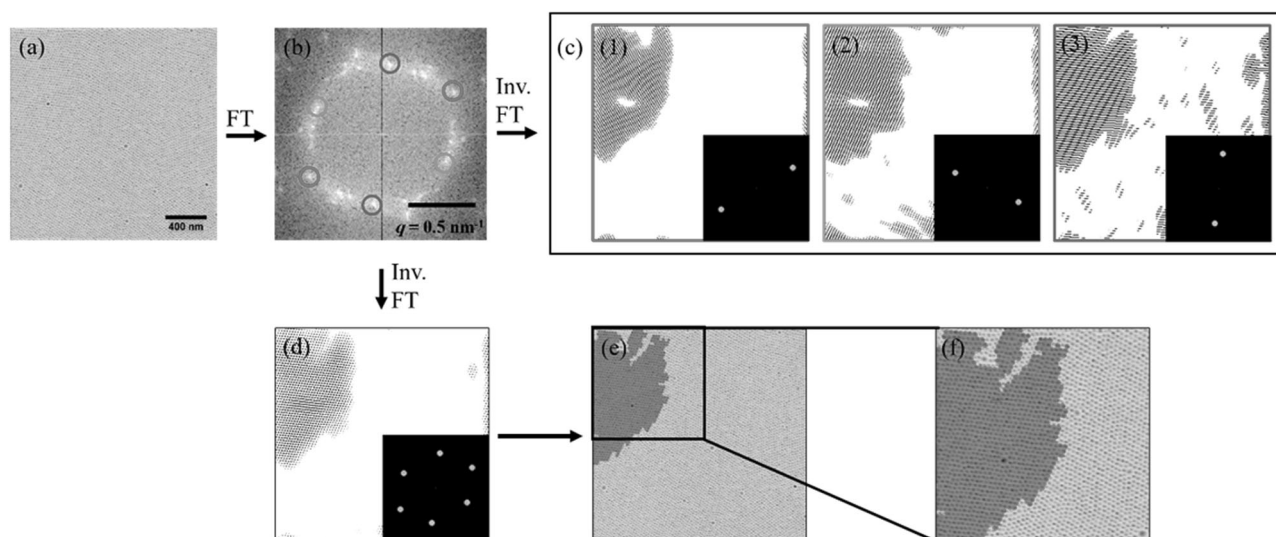


Fig. 2 Image analysis steps to evaluate the grain size from the AFM phase images (Method I). **(a)** AFM phase image, **(b)** FT pattern, **(c)** Inverse FT of each pair of spots ((1), (2), & (3) by using a mask to select the red, green, and blue circles shown in **(b)**; respectively), **(d)** Inverse FT by using a mask to select the six spots, **(e)** The identified grain overlapped with the AFM phase image, and **(f)** Enlarged-view of **(e)**

arrangement of the PS spherical microdomains was generated, as shown in Fig. 1a, in which a ring peak is ambiguously observed in the FT pattern. To induce ordering, the as-spin-coated specimen was subjected to thermal annealing at 140 °C (higher than the glass transition temperature (T_g) of PS and below the T_{ODT}). As shown in Fig. 1b, after only 5-min annealing, regular ordering of the spheres can be observed. By increasing the annealing time, the regularity can be improved (Fig. 1c–j). The FT spots become more discrete as a function of the annealing time. Furthermore, the appearance of the higher order spots clearly indicates higher regularity in the ordering of the spheres. Actually, the higher order spots can be seen in the FT patterns for the images in Fig. 1f–j. Finally, approximately six spots (of the first-order reflections) are observed in Fig. 1i and j, indicating that the grains became very large. Thus, the FT pattern can be used as an indicator of the grain growth. In other words, if the grains are small, then the FT pattern shows many spots, which is indicative of the early stage of thermal annealing (Fig. 1b–e). Therefore, it is clear that the grains grow with increased annealing time. By using the FT pattern, the grain size on the free surface can be evaluated quantitatively by image processing of the AFM images.

The method of grain identification employed in the current study has already been reported by Ohnogi et al. [17], and the method is briefly summarized in Fig. 2. After conducting FT of the AFM phase images (Fig. 2b), the inverse FT by using a mask with six holes is conducted. The set of six spots selected by the mask is indicated with the colored circles shown in Fig. 2b, as an example among the enormous number of combinations, six spots

could be selected in the case of the FT pattern in Fig. 2b. Notably, the set of six spots should come from a single grain. To confirm whether the set of six selected spots is correct, we selected three pairs from the six spots and conducted the inverse FT on each of the pairs. As shown in Fig. 2c, we can see that the grains are in the same location. This clearly demonstrates that the selection of the six spots as one set is correct, and the spots are from a single grain. Therefore, the inverse FT can be conducted by using a mask with six holes, as shown in Fig. 2d. Finally, the identified grain is overlapped onto the original AFM image, as shown in Fig. 2e (more concretely in the magnified view of Fig. 2f), which enables us to directly confirm the validity of the grain identification by this method. Hereafter, this method is referred to as Method I.

When there are many tiny grains in the original AFM image, Method I is ineffective. This is because the corresponding FT pattern would be a donut-shaped ring without any spots. Therefore, an alternative method is required. To overcome this problem, the following image processing is proposed (Method II). Figure 3 shows the steps of this method. The same AFM phase image shown in Fig. 2a was used to check the validity of this method, and the mask (schematically shown in the inset of the inverse FT pattern) for the inverse FT has a donut-shaped hole, which covers all the spots appearing in the FT pattern. After conducting the inverse FT, the “Ultimate Points” command in ImageJ software was used such that the center of each microdomain can be identified as shown in Fig. 3a. Then, these points can be connected with lines using the “Watershed” command in ImageJ software, which results in a mesh pattern. To check the validity of the mesh pattern as a representative

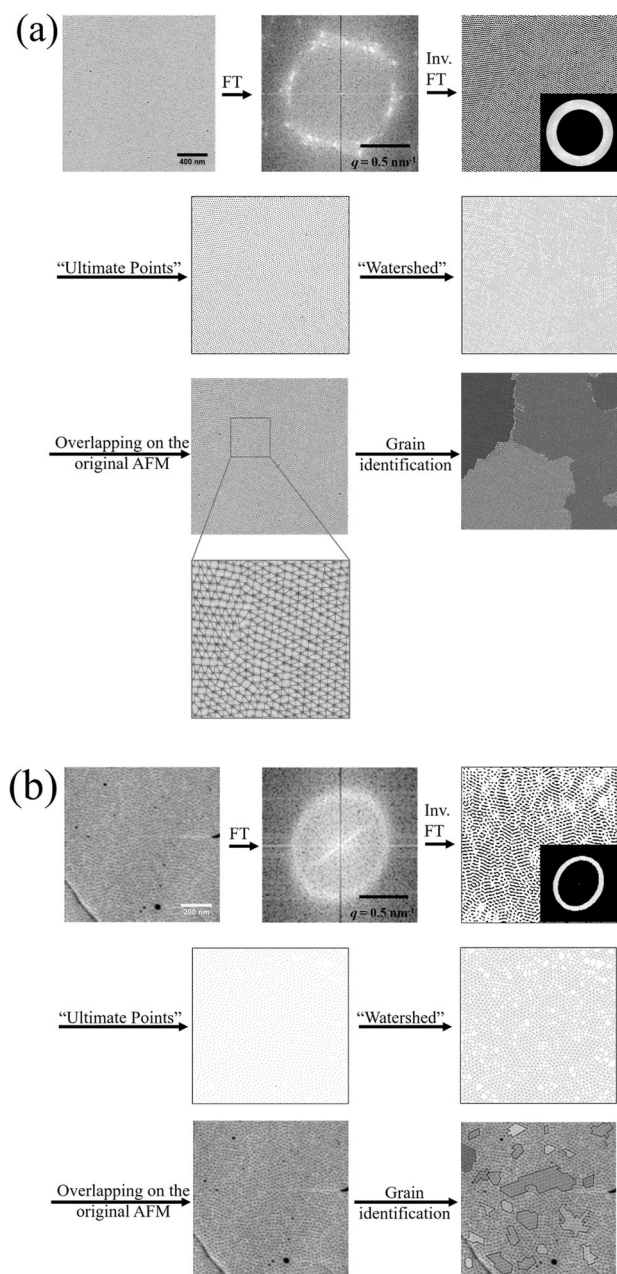


Fig. 3 Image analysis steps to identify grains from the AFM phase images (Method II). **(a)** Demonstration by using the same image used in Fig. 2. **(b)** Demonstration by using the original AFM phase image containing many small grains

of the original AFM image, good overlapping of these images was observed, as shown in Fig. 3a, which confirms the validity of Method II. The mesh pattern is helpful for identifying grains because approximately straight lines can be drawn along the mesh lines. If we can find a single triangle lattice, this region can be considered a single grain. Finally, we can identify four grains in the original AFM image shown in the final image of Fig. 3a, and a grain with the same shape as what was found in Fig. 2e can be identified in the upper-left corner. For the AFM images

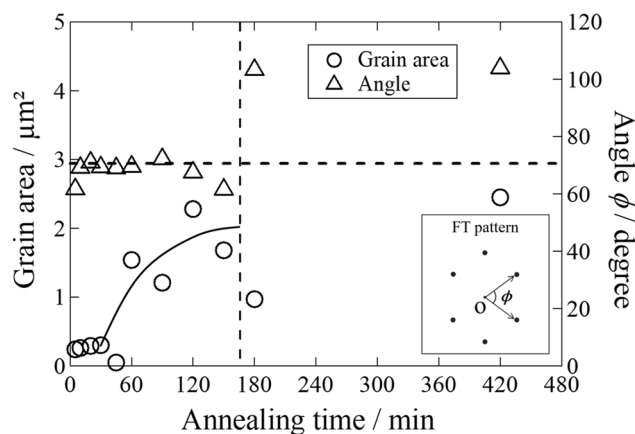


Fig. 4 Plots of the area of the largest grain identified in the AFM image (left axis) and the largest angle ϕ (its definition is schematically shown in the inset) between the two position vectors of the first neighboring spots appearing in the FT pattern (right axis) as a function of annealing time

containing tiny grains, as shown in Fig. 3b, the same procedure has been applied. In addition, the tiny grains were identified as shown in the final image of Fig. 3b. Here, the various colors correspond to each grain identified. It should be noted here that the grains are not in direct contact. In other words, the small grains exist independently and are embedded in the region where spherical microdomains are not regularly ordered.

Figure 4 shows the areas of the largest grains identified in the AFM images using Method I and II as a function of annealing time (open circles). The data points are scattered because of the experimental procedure (the AFM observation). Namely, we used different specimens for different durations of thermal annealing. Furthermore, when the grains become bigger than the AFM observation area, problems arise. Actually, for the grain shown in the upper-left corner of the image in Fig. 2e, it is impossible to evaluate the real grain size because of truncation at the edge of the image. Nevertheless, it can be seen that the grains in the early stage of annealing grow slowly for 30 min, and then they grow rapidly during further annealing up to ~90 min. Finally, the grain size seems to become constant after 166 min of annealing (vertical broken line). The reason for drawing this vertical broken line at an annealing time of 166 min is that we can distinguish the spherical microdomain arrangement on the (110) plane of the bcc lattice when the annealing time was <166 min, where the set of six spots in the FT pattern forms a skewed hexagon with the ratio of the short to long edges being equal to 1.15 [14, 18, 19]. In this case, the angle ϕ between the two position vectors of a pair of neighboring spots which are closest to the origin of the FT pattern (the definition of ϕ is schematically shown in the inset in Fig. 4) is 70.6°, which was confirmed by the open triangles with the broken

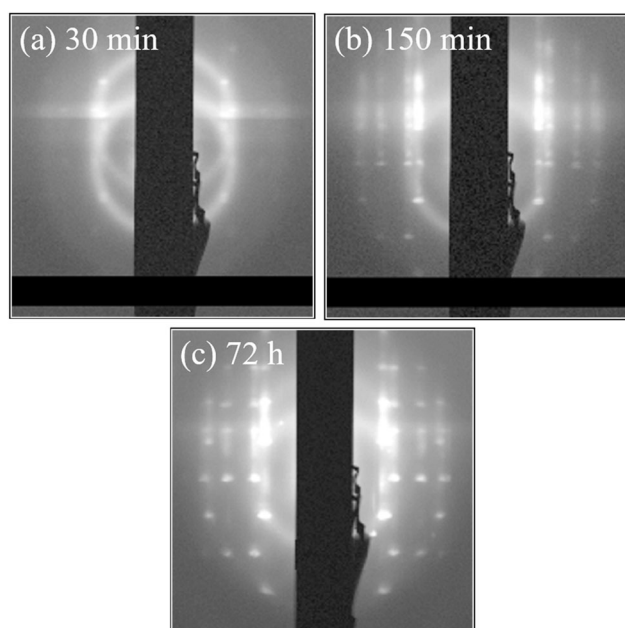


Fig. 5 Change in the 2d-GISAXS patterns as a function of thermal annealing time at 140 °C for the SEBS-8 specimens with a thickness of 1.4 μm . (a) 30-min, (b) 150-min, and (c) 72-h thermally annealed specimens. These 2d-GISAXS patterns are depicted according to a gray scale of the logarithmic intensity

horizontal line ($\phi = 70.6^\circ$) in Fig. 4 at annealing times less than 166 min. In contrast, a much larger angle ϕ was found for longer annealing times, 180 and 420 min. This indicates that spheres are located on a heavily deformed hexagonal lattice, which may be due to an unknown error of the AFM observation. In fact, for longer annealing time (72 h) the unfavorable large deformation was not detected in the GISAXS measurements (Fig. 6), which showed a ratio of 1.15 peak positions (which will be discussed later in detail).

As mentioned above, the (110) planes are oriented parallel to the free surface of the specimen [10], which was confirmed by AFM (Figs. 1 and 4) in the current study. Since the regular ordering of the spherical microdomains on the (110) plane near the free surface can be directly confirmed by the 2d-GISAXS measurements [18, 19], we conducted the 2d-GISAXS measurements at room temperature. For this purpose, we used the specimens that were spin-coated on silicon wafers and thermally annealed for different durations. As shown in Fig. 5, the 2d-GISAXS patterns (according to a gray scale of the logarithmic intensity) changed as a function of the thermal annealing time from 30 min to 72 h. Note that although the pattern is not shown, in the as-spin-coated state, no spots were observed. After 30 min of annealing, as shown in Fig. 5a, spotty peaks appeared. After further annealing up to 72 h, the number of the spots increased. This is in accordance with the results of the edge-view 2d-SAXS measurements (Fig. 8, shown later). Hereafter, we only discuss the

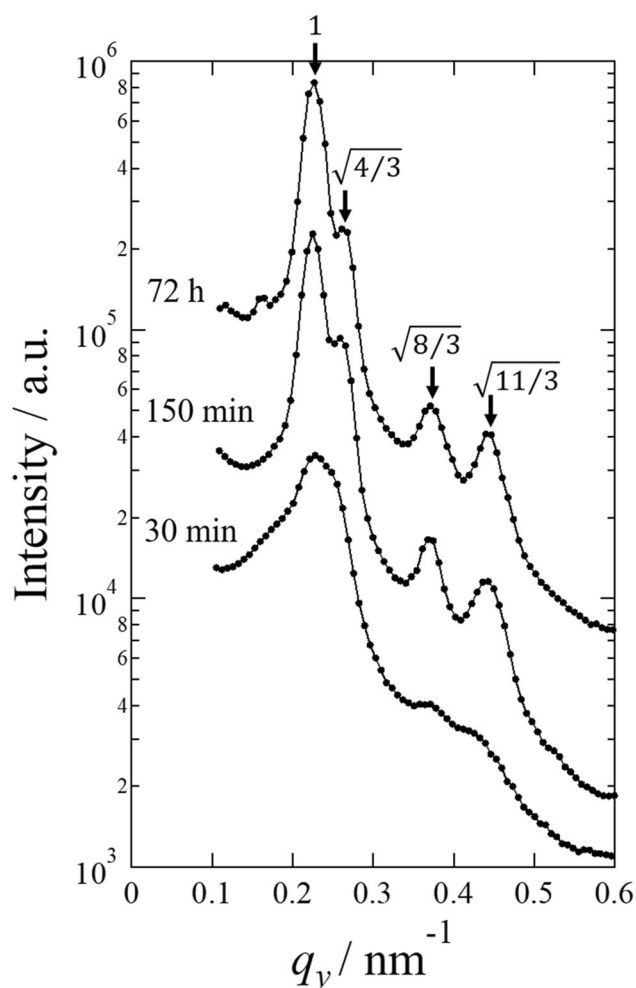


Fig. 6 Change in the 1d-GISAXS profiles converted from the 2d-GISAXS results presented in Fig. 5 (at the Yoneda wing), as shown in the plot of the semi-logarithmic scattering intensity as a function of q_y

evolution of peaks from the outermost layer by examination of the 1d-GISAXS profile at the Yoneda wing (the in-plane profile). Note that the Yoneda wing is located in the range of $0.19 < q_z < 0.20 \text{ nm}^{-1}$. In Fig. 6, the change in the 1d-GISAXS profiles at the Yoneda wing as a function of q_y is shown for various durations of annealing. Here, q_y and q_z denote the magnitudes of the scattering vectors as $q_y = \frac{2\pi}{\lambda} \sin 2\theta \cdot \cos \alpha_f$ and $q_z = \frac{2\pi}{\lambda} (\sin \alpha_i + \sin \alpha_f)$, where 2θ and α_f are the in-plane and out-of-plane scattering angles (i.e., the scattering angle components on the planes parallel and perpendicular to the specimen surface, respectively). Since the AFM image shown in Fig. 1a for the as-spin-coated specimen exhibits no regular ordering of the spherical microdomains, the appearance of the broad first-order peak in the GISAXS profile (not shown in Fig. 6) is as expected. After 30 min of annealing, a small shoulder appeared beside the first-order peak. This shoulder position is similar to that of the side peaks appearing in the profiles of the specimens annealed for longer periods. Furthermore, two small peaks

can be detected at $q_y = 0.38$ and 0.43 nm^{-1} in the profile of the 30 min annealed specimen. These are considered to be the same peaks that appeared in the profiles of the specimens annealed for longer periods. By further increasing the annealing time, these peaks became more evident, clearly indicating the regular ordering of the spherical microdomains. Note that for both the 150-min and 72-h annealed specimens, the peak positions can be assigned to 1: $\sqrt{(4/3)}$: $\sqrt{(8/3)}$: $\sqrt{(11/3)}$ with respect to the q_y value of the first-order peak. Therefore, these peaks in the in-plane profile can be attributed to the bcc lattice peaks of the planes perpendicular to the surface of the specimen [14, 18, 19]. The first- and second-order peaks correspond to $2d_{112}$ and d_{110} spacings, respectively, according to our previous paper [14]. The fact that these lattice peaks are observed in the in-plane profile indicates that the (110) plane, which is perpendicular to these planes ($\bar{1}12$ and $\bar{1}10$ planes), is parallel to the surface of the specimen. Thus, the appearance of the lattice peaks in the in-plane profile (as indicated by the arrows in Fig. 6) clearly confirms the ordering of the spherical microdomains on the (110) plane of the bcc lattice.

We now discuss the results of the conventional 2d-SAXS measurements of the annealed specimen (annealed for 10 h at 140°C). Figure 7 depicts two views of the 2d-SAXS patterns with schematic illustrations explaining the through and edge-view geometries. Note here that q denotes the magnitude of the scattering vector as defined by $q = \frac{4\pi\lambda}{\sin^2\theta}$ with θ being the scattering angle. Here, the thin-film specimen, having a thickness of $2 \mu\text{m}$ (blue-colored sheet in the schematics), was peeled off of the silicon wafer and transferred to a polyimide (Kapton) film (orange-colored sheet in the schematics) with a thickness of $25 \mu\text{m}$. Note that in the edge view, a long beam stopper was used to hide the strong streaks of the total reflection of the incident X-ray beam from the surface of the specimen and the Kapton film. The through view, in which the incident X-ray beam is parallel to the film normal, shows almost isotropic ring peaks for the

{110} and {200} reflections (the bcc lattice peaks with relative q positions of 1: $\sqrt{2}$), indicating almost no preferential orientation of the bcc lattice with respect to the normal of the film specimen. Although the peak intensity as a function of the azimuthal angle is not completely constant, suggesting a weak preferential orientation, the origin of such orientation is unknown. It is noted here that after 10 min of annealing, the FT patterns show clear spots, as shown in Fig. 1c–f, while the through-view SAXS pattern does not show such spots. This is simply because the sizes of the specimens subjected to the experiments are much different. Namely, the AFM micrographs show a much smaller area, while the SAXS measurements gives averaged structural information over the area of the specimen irradiated by the incident X-ray beam ($0.3 \text{ mm}\phi$). Even though the localized area exhibits a single (or several) grain(s), the grains are much smaller than the size of the incident X-ray beam. Therefore, the resulting SAXS pattern is randomized due to the random orientation of the grains (as shown in Fig. 4 of our previous publication [10]). On the other hand, the edge view, in which the incident X-ray beam is perpendicular to the normal of the film, shows a well-ordered spot pattern with {110}, {200}, and {211} reflections of the bcc lattice with relative q positions of 1: $\sqrt{2}$: $\sqrt{3}$ from the origin of the 2d-SAXS pattern. These crystallographic spots can be confidently assigned based on the orientation of the (110) plane parallel to the surface of the silicon wafer or the free surface, as was reported in our previous publication [10].

To determine the mechanism of grain growth in the thickness direction, we conducted time-resolved 2d-SAXS edge-view measurements as a function of thermal annealing time. The SAXS measurements were conducted at room temperature using the same annealed specimen. Namely, once the SAXS measurement was completed for the as-cast specimen (Fig. 8a), the specimen was then thermally annealed for 28 min in an N_2 -purged oven. After quenching to room temperature, the annealed specimen was again subjected to the SAXS measurement with the same position of the specimen being illuminated by the incident X-ray beam. This procedure was repeated many times to measure the 2d-SAXS patterns as a function of the annealing time, as shown in Fig. 8 (according to a gray scale of the logarithmic intensity). The 2d-SAXS pattern for the as-cast specimen displays an elliptical pattern, which is considered to be due to the effect of solvent evaporation [20]. However, after 28 min of thermal annealing, the 2d-SAXS pattern became round, as shown in Fig. 8b. Although the peak is not completely round, the difference in the peak positions in the q_{\parallel} and q_{\perp} directions is only 4 pixels ($\pm 4.8\%$ difference). Here, q_{\parallel} and q_{\perp} denote the scattering vectors parallel and perpendicular to the surface of the film specimen, respectively. Therefore, the ring peak can be considered to be

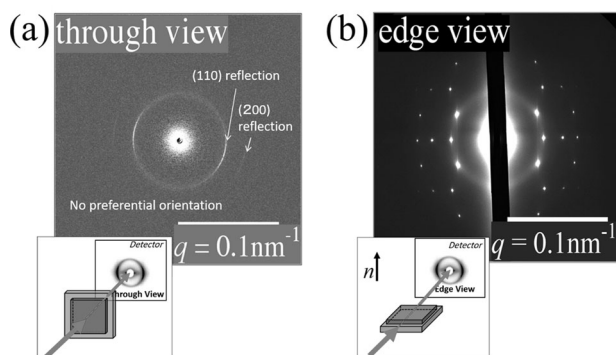


Fig. 7 Through and edge views of the 2d-SAXS patterns for the SEBS-8 specimen annealed at 140°C for 10 h (the thickness is $2 \mu\text{m}$). The specimen shows no preferential orientation in the through view (a), while a well-ordered spot pattern is visible in the edge view (b)

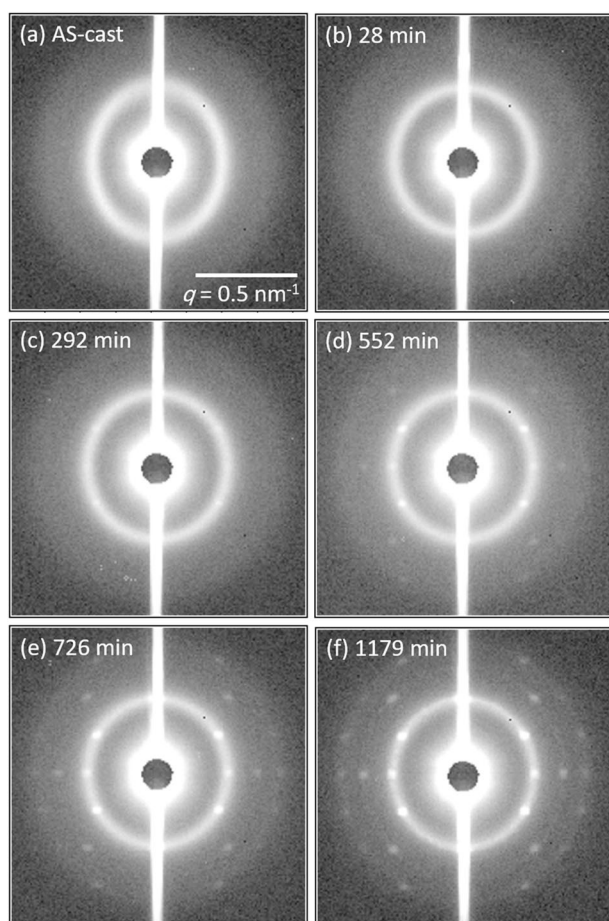


Fig. 8 Changes in the edge-view 2d-SAXS patterns as a function of thermal annealing time at 140 °C for the SEBS-8 specimen with a thickness of $43.3 \pm 2.2 \mu\text{m}$; **(a)** as-cast specimen, **(b)** 28, **(c)** 292, **(d)** 552, **(e)** 726, and **(f)** 1179 min annealed specimens. **(a)**, **(b)** The scale bar shown for the as-cast specimen is applicable to all of the patterns. These 2d-SAXS patterns are depicted according to a gray scale of the logarithmic intensity

round for annealing times >28 min. While only the ring peak was observed for the specimen annealed for 28 min, the spot pattern was observed after 292 min of thermal annealing, as shown in Fig. 8c, which is a result of the orientation of the (110) plane of the bcc lattice parallel to the surface of the film specimen, and this has been reported previously [10]. For longer annealing times, the spots became more obvious, as shown in Fig. 8d–f. In particular, spots of the two higher order reflections with relative q positions of $\sqrt{2}$ and $\sqrt{3}$, reflected from the {200} and {211} planes, can be clearly seen in Fig. 8e and f. This clearly suggests that the bcc ordering of the spheres becomes very regular, which is in good agreement with the GISAXS results. Furthermore, the appearance of the spot peaks clearly indicates the spontaneous orientation of the (110) plane parallel to the surface of the film specimen. However, it is notable that the ring peak remained. The coexistence of the ring peak with the spot peaks suggests

that the two representative states coexist in the film specimen. One is the region that contains grains without any preferential orientation of the (110) planes, and the other contains the (110) planes that are parallel to the free surface of the specimen or to the surface in contact with the substrate (the Kapton film) surface. In fact, in our previous publication, we successfully confirmed the existence of such oriented layers in the vicinity of the free surface and the surface in contact with the substrate by employing a special technique in the 2d-SAXS measurements (see our previous publication [10] for the special technique). Therefore, the three-layered model (as schematically shown in Fig. 9b) can be considered, and based on this model, it is possible to evaluate the thickness of the oriented layers in the free surface region and in the opposite region in contact with the Kapton film. Although we did not conduct AFM observations of the surface of the specimen directly in contact with the Kapton film, it can be assumed that grain coarsening also takes place on that surface because the (110) planes parallel to the surface of the Kapton film were found to be oriented based on special SAXS measurements, as reported in our previous paper [10]. Those two layers near the free surface and the substrate surface grow individually by thermal annealing from the initial grain-free state. In other words, such oriented layers can be considered to be initiated at the surface and then grow toward the interior of the specimen. Therefore, the interference of grain coarsening between these two layers is not a concern. Hereafter, the total thickness of the two layers is evaluated according to the following procedure, and the evaluated values were divided by two to discuss the increase in the thickness of the oriented layer on one side as a function of annealing time. Note that the increase in the thickness of the oriented layer can be considered to be grain growth in the thickness direction.

Figure 9a is a reproduction of Fig. 8f, and by taking this image as an example, we can explain our method of evaluating the total thickness of the oriented layers near the free surface and near the surface in contact with the Kapton film (as schematically shown in Fig. 9b [10]). Here, the red color indicates the portion where the (110) planes are oriented parallel to the surface, while the other colors indicate other orientations. Thus, the oriented layers at both surfaces are colored in red, while in the interior of the specimen, we intended to show existence of small grains with different orientations by using many different colors. It is possible to color some of the interior grains red because (110) planes oriented parallel to the surface should exist also in the intermediate layer of the specimen. Since the thickness of the specimen ($\sim 43 \mu\text{m}$) is less than the diameter of the incident X-ray beam ($\sim 300 \mu\text{m}$), the incident beam thoroughly illuminates the three layers. Therefore, the peak intensity is proportional to each layer thickness. Based on

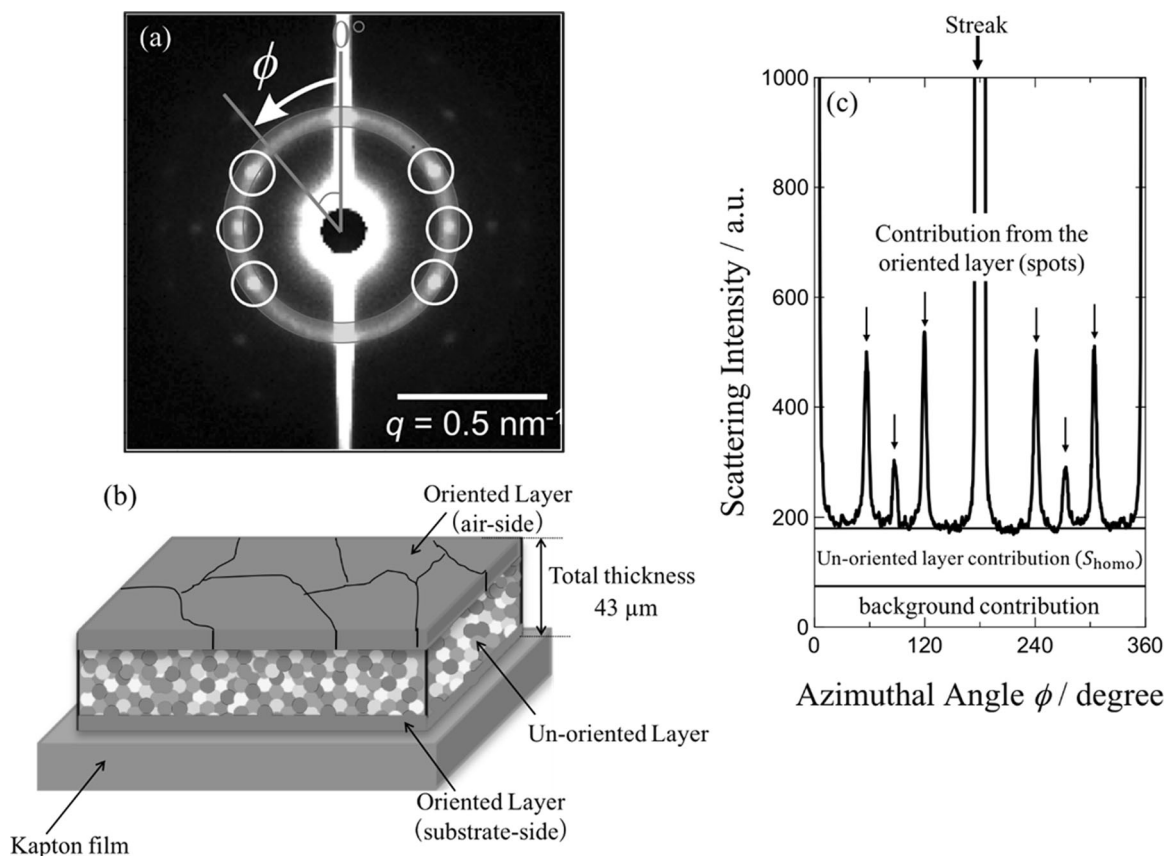


Fig. 9 (a) 2d-SAXS pattern (edge view) obtained from the SEBS-8 specimen thermally annealed for 1179 min showing the spots (from the oriented layers as schematically illustrated in (b)) with the ring peak (from the un-oriented small grains in the intermediate layer in (b) [10]). (c) A plot of the integrated scattering intensity (in the q range from 0.227 to 0.321 nm^{-1}) as a function of the azimuthal angle (its definition is shown in (a)). Six sharp peaks and the constant intensity correspond to the spots and the ring peak, respectively, in (a). The background scattering inevitably contributes to the constant intensity

this idea, we can evaluate the total thickness of the oriented layers in the free surface region and the opposite region in contact with the Kapton film. First, the spot peaks must be differentiated from the ring-shaped peak. Figure 9c shows the integrated scattering intensity as a function of the azimuthal angle ϕ . Here, the scattering intensity in the q range from 0.227 to 0.321 nm^{-1} , which completely covers the first-order peak (the reflection from the $\{110\}$ planes), was integrated. Note that the definition of ϕ is shown in Fig. 9a. In Fig. 9c, the six sharp peaks correspond to the six spots in Fig. 9a, and the constant intensity corresponds to the ring-shaped peak and the background (from the empty cell, the Kapton film, and the air). The background intensity (I_b) was evaluated from the 1d-SAXS profile by peak decomposition as the following:

$$I_b = aq^n + b \quad (2)$$

where a , b , and n are constants. Then, the contribution of the intermediate (un-oriented polygrain) layer (S_{homo}), shown in Fig. 9b, to the scattering intensity can be

evaluated by subtracting the background intensity, as indicated by the rectangular area in Fig. 9c. The contribution of the oriented layers (S_{ori}) can be evaluated from the summation of the scattering intensities of the six peaks (S_{sum}) by assuming the following relationship:

$$S_{\text{ori}} = S_{\text{sum}} \times 1.2 \quad (3)$$

S_{sum} is multiplied by 1.2 because the two spots, which should appear in the direction perpendicular to the film specimen ($\phi = 0^\circ$ and 180°), are completely overlapped by the strong streaks due to the total reflection of the X-ray beam from the surface of the film specimen and the Kapton film. Since the spots that can be assigned to the (110) and $(\bar{1}\bar{1}0)$ planes among the 12 possible $\{110\}$ planes [10] are hidden, we can only sum the peak areas of other planes. To compensate for the missing contributions from the two hidden peaks, the sum of the 10 visible peaks should be multiplied by a factor of 1.2. This factor allows us to formulate Eq. 3. As mentioned in our previous publication [10], the spots appearing in the equatorial direction ($\phi = 90^\circ$ and 270°) are assigned to the $(\bar{1}10)$ and $(1\bar{1}0)$

planes, respectively. On the other hand, the four spots appearing in the azimuthal angles ($\phi = 60^\circ, 120^\circ, 240^\circ,$ and 300°) are considered to be the overlap of reflections from two different pairs of planes with the same azimuthal angle. In our previous publication [10], the spots appearing at $\phi = 60^\circ$ were attributed to the overlapping reflections from the (101) and $(\bar{1}01)$ planes under the conditions that the (110) planes are oriented parallel to the surface and that the orientations of the other planes are homogeneous with respect to the $\langle 110 \rangle$ direction, which is parallel to the normal of the film specimen (see Fig. 4 of ref. 10). This is why the area of the peak appearing at $\phi = 60^\circ$ is a double of that of the peak appearing in the equatorial direction, as shown in Fig. 9c. The conditions are the same for the peaks appearing at $\phi = 120^\circ, 240^\circ,$ and 300° . Thus, in total, eight reflection planes contribute to those four spots, while two reflection planes contribute to the two spots appearing in the equatorial direction. Therefore, the six spots appearing in the 2d-SAXS pattern (other than the two spots appearing in the meridional direction) can be attributed to ten $\{110\}$ planes (other than (110) and $(\bar{1}\bar{1}0)$ as mentioned above).

Finally, the total thickness of the oriented layers (d_{ori}) can be evaluated using S_{ori} and S_{homo} , as given by the following:

$$d_{\text{ori}} = \frac{S_{\text{ori}}}{S_{\text{ori}} + S_{\text{homo}}} \cdot d_{\text{tot}} \quad (4)$$

where d_{tot} is the thickness of the film specimen.

Thus, the calculated values of d_{ori} can be a measure of the grain size in the thickness direction, as mentioned above. In fact, half d_{ori} can be considered as the grain size in the thickness direction if the thickness of the oriented layer near the free surface and that near the surface in contact with the substrate are identical to each other. However, it should be noted here that there is a possibility of overestimation of the layer thickness. This is because the small grains, that have the same orientation as the (110) planes parallel to the surface in the intermediate layer of the specimen (the small red circles in the illustration in Fig. 9b), contribute to the intensity of the spot peaks as specified with arrows in Fig. 9c. Since these contributions are not attributed to the oriented layers at the surfaces, the evaluated value of S_{sum} is overestimated, ultimately causing an overestimation of d_{ori} .

The double logarithmic plot of half d_{ori} as a function of the annealing time is shown in Fig. 10 together with the grain size on the free surface of the specimen as evaluated by AFM. The latter values were evaluated as the diameter of the equivalent circle having the same area as the grain (the grain area is plotted in Fig. 4). By assuming power-law growth behavior of the grain size as a function of annealing time (t):

$$\text{Grain size} \propto t^\alpha \quad (5)$$

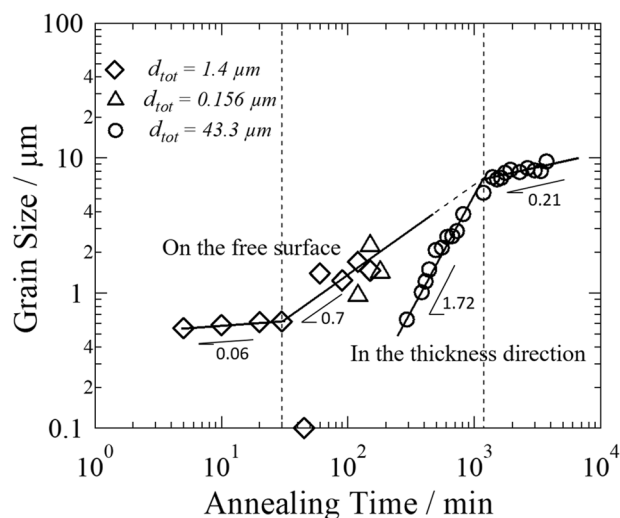
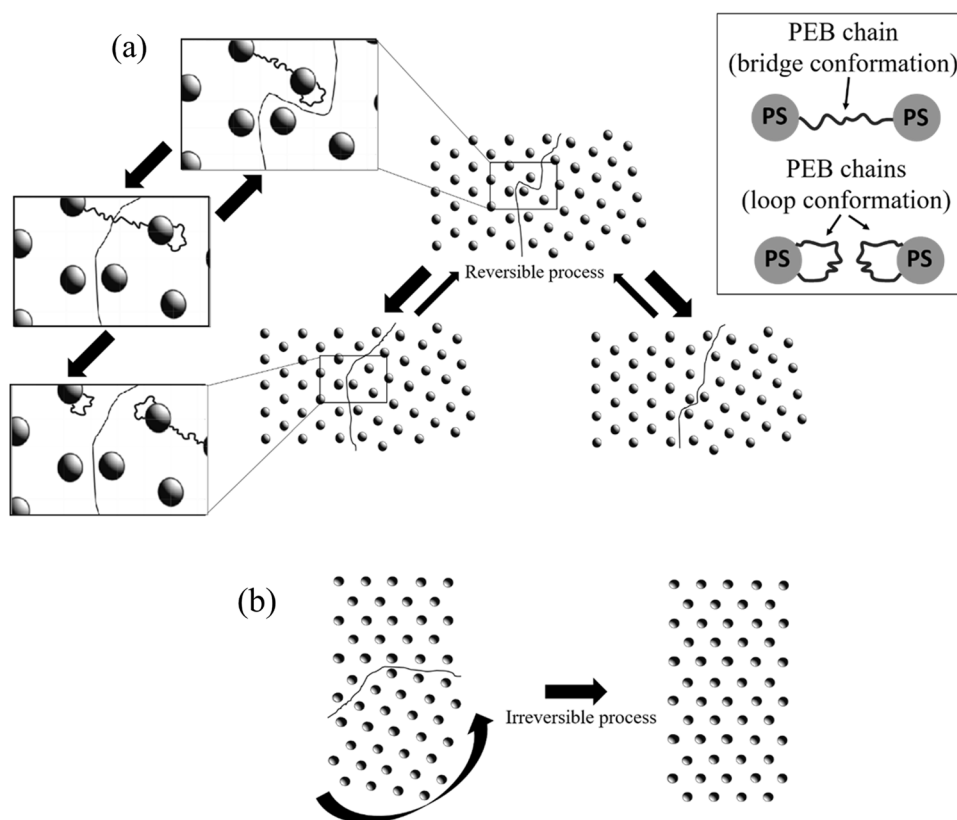


Fig. 10 Double logarithmic plots of the grain size on the free surface and in the thickness direction as a function of thermal annealing time

the growth exponent α can be evaluated. In the early stage of annealing, the grain on the free surface grows very slowly with $\alpha = 0.06$, which may imply that the grain cannot easily grow due to strong growth competition among grains of similar sizes. In contrast, the grains became capable of growing rapidly with $\alpha = 0.7$ in the annealing time range of 30–200 min, although the data show substantial scattering around the approximated line. The AFM visualizations are limited to a localized area, so the statistical accuracy of the results is low. Moreover, a large grain cannot be completely visualized by the AFM observation area. Therefore, the observed grain is truncated. This results in an underestimation of grain size. In such situations, a growth exponent $\alpha \approx 0.7$ can be obtained. Note that the growth exponent value of 0.7 can be attributed to an intermediate behavior between two growing mechanisms: a random process ($\alpha = 1/3$) and a deterministic process ($\alpha = 1$; this is the process affected by hydrodynamics) [21–31]. The random process, which is schematically shown in Fig. 11a, may take a long time because each spherical microdomain can change its position from one grain to another. Due to the bridge conformation of the middle PEB block, this process is considered reversible. Notably, there is an almost even chance of finding the middle chain of triblock copolymer in either the bridge or loop conformation [32]. When the transformation from the bridge to loop conformation is complete, the process of changing the position of each spherical microdomain from one grain to another is also complete. After this process occurs many times, the larger grains grow, and the smaller grains shrink. In contrast, Fig. 11b shows a possible explanation for the rapid grain growth involving the rotation of the smaller grains. Because this process can be considered as the one

Fig. 11 Plausible mechanisms of grain growth. **(a)** Slow process in which each microdomain changes its position from one grain to another (random process). Changing only the position of the microdomain does not mean the grain growth is complete because the position may change back as long as the bridge conformation of the PEB chain is conserved. True completeness of the grain growth may be achieved by changing from the bridge to loop conformations. **(b)** Fast growth process in which the small grains rotate by a hydrodynamic effect, resulting in their incorporation into larger neighboring grains



governed by hydrodynamics, a growth exponent of $\alpha = 1$ is expected.

For the grain growth in the thickness direction, the power-law behavior is clearly confirmed with $\alpha = 1.72$ ($t < 1180$ min). We reported $\alpha = 1.5$ in our previous publication [10]. This new result reported herein is more reliable than the previous result because of a very small number of data points were used and different specimens were used for the thermal annealing tests in our previous publication, which found $\alpha = 1.5$. Although the grain growth in the thickness direction was rapid, after ~ 1000 min of thermal annealing, a deviation in the plot from the power-law behavior with $\alpha = 1.72$ can be observed. In fact, the mode of the grain growth appeared to slow with $\alpha = 0.21$ at an annealing time of 1180 min (the vertical broken line in Fig. 10). Furthermore, it seems that the grain size is larger in the horizontal direction than in the thickness direction (namely, the grains are pancake shaped); however, a direct comparison may not be appropriate because the substrates are different from each other. In fact, for the AFM observations, a Si wafer was used, while for the SAXS measurements, Kapton film was used. The difference in the type of substrates may affect the grain coarsening. Therefore, a direct comparison is not appropriate between the grain size in the horizontal direction as evaluated by AFM observations and that in the thickness direction as evaluated by SAXS measurements. Nevertheless, it is interesting that the

horizontal grain size increases towards the same value as the vertical grain size ($9.5 \mu\text{m}$) after 1180 min of annealing.

Again, it should be noted that the value of the exponent α for the growth behavior of the grains in the thickness direction is much higher than $\alpha = 1$. It is impossible to visualize a growth mechanism of the grain because $\alpha = 1$ is the maximum value in the conventional framework of the growth of domains and droplets [21–31]. This may indicate that a new framework is required to explain the grain growth behavior in the spherical microdomain system as reported in the current study. Another notable finding is that the thickness of the oriented layer is as thick as $9.5 \mu\text{m}$, which is substantially larger than the reported values ($1\text{--}2 \mu\text{m}$) [33]. This large propagation distance in the surface-induced orientation of the microdomains might indicate that grain growth serves as a propagator for the regular ordering of spherical microdomains and the orientation of the lattice. In our previous paper, we reported $\alpha = 0.45$ for the perpendicularly oriented cylinder system both on the free surface and in the interior of the specimen. Furthermore, the grain size is $< 2 \mu\text{m}$. These results are noticeably different from the above-mentioned results obtained in the current study for the spherical microdomain system. The same values were found for α for the grain growth on the free surface and in the interior of the specimen because the grain growth in the same direction (which is parallel to the surface) was examined for the

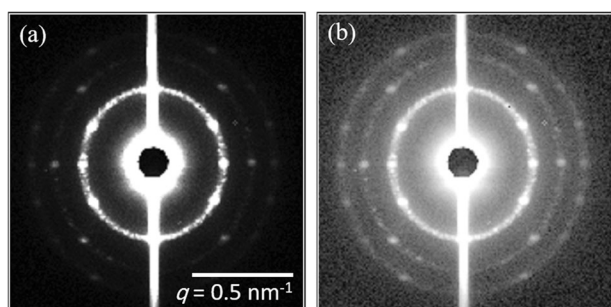


Fig. 12 Edge-view 2d-SAXS pattern for the specimen (thickness of $43.3 \pm 2.2 \mu\text{m}$) after 3713 min of thermal annealing at 140°C . The spots appearing along the ring pattern, other than the main spots of the $\{110\}$ planes, indicate that the grains had grown even in the intermediate layer of the specimen. **(a)**, **(b)** A gray scale of the scattering intensity and of the logarithmic intensity, respectively

previous case (the perpendicularly oriented cylinder system); however, in the current study, the evaluation of the grain size was conducted separately on the free surface and in the interior of the specimen. In contrast, for the spherical microdomain system, we determined the grain size separately in the different directions, perpendicular and parallel to the surface of the specimen. This may be why we obtained substantially different values for α . Finally, a much larger grain size was observed for the spherical microdomain system in the current study even when compared to the perpendicularly oriented cylinder system. This may be due to the discrete shape of the microdomains. In other words, compared to the spherical microdomains, regular ordering is not easily propagated in the case of the cylindrical microdomains due to their continuous shape.

Finally, it is interesting to discuss the 2d-SAXS pattern observed after long annealing time (3713 min), as shown in Fig. 12. Figure 12a and b shows a gray scale of the scattering intensity and that of the logarithmic intensity, respectively. It is clear that the isotropic ring peak evolved into a speckling pattern. Since the azimuthal angles of the spots appear at random, none of the $\{110\}$ planes are parallel to the surface. Therefore, the 2d-SAXS pattern suggests that some of the grains became very large even in the intermediate layer of the specimen. It is, of course, reasonable to consider that the grains can grow even in the intermediate layer. However, in the meantime, the oriented layers grow in the thickness direction and may ultimately prevail over the intermediate layer. There would be growth competition between the grains present in the intermediate layer and those in the oriented layers growing in the thickness direction. The growth rate is considered to be much higher for the latter case. In this regard, it seems that there is no chance for the grains in the intermediate layer to grow quite as large. However, for a comparatively thick specimen, the time required for total invasion of the

intermediate layer is much longer, which would give the grains in the intermediate layer a chance to grow. In case of grains that had already grown quite large, it is not possible for the oriented layer growing from the surface along the thickness direction to incorporate such advanced grains in the intermediate layer because those grains are already large enough to resist invasion by the oriented layers. This may be an explanation for the observed speckles in the 2d-SAXS pattern shown in Fig. 12 after an extended annealing time. Furthermore, this may also explain the spontaneous change in the grain growth mode in the thickness direction after 1180 min, as shown in Fig. 10.

Conclusion

The grain size on the free surface was quantitatively evaluated using AFM combined with image processing. Then, it was found that the grain growth in the direction parallel to the free surface was very slow in the early stage of thermal annealing, which may be due to strong growth competition among small grains of similar sizes. Subsequently, the grain growth shifted to a rapid growth mechanism with a power-law relationship (grain size $\sim t^\alpha$, with $\alpha = 0.7$) after ~ 30 min. From the value of the growth exponent α , the grain growth mechanism can be considered to fall between the random and deterministic processes. As a plausible model, the rotation of smaller grains is proposed as a part of the fast growth mechanism. On the other hand, for the thickness direction, a much bigger value of α ($\alpha = 1.72$) was obtained based on the evaluated grain size using the 2d-SAXS edge-view measurements. Compared to the previously reported value of $\alpha = 1.5$, the result reported here is more reliable because a larger number of data points were used in the current study and because the same specimen was used throughout the thermal annealing tests. Nevertheless, it is impossible to consider the growth mechanism of the grain within the conventional framework of the growth of domains and droplets [21–31]. This may suggest that a new framework is required to explain the grain growth behavior in the spherical microdomain system. Another notable finding is that the thickness of the oriented layer is as thick as $9.5 \mu\text{m}$, which is substantially larger than the values reported for the propagation distance for the surface-induced orientation of spherical microdomain lattice [33]. This may indicate that grain growth serves as a propagator for the regular ordering of spherical microdomains and orientation of the lattice. Finally, a much larger grain size was observed for the spherical microdomain system in the current study than what was reported for the perpendicularly oriented cylinder system [3]. This may be due to the discrete shape of the microdomains. In other words, compared to the spherical microdomains, regular ordering is more difficult to

propagate in the case of cylindrical microdomains due to their continuous shape.

Another significant finding was that the rapid grain growth in the thickness direction was slowed down. Grain growth in the intermediate layer of the specimen may play an important role in this slowing-down phenomenon. Since the 2d-SAXS pattern observed after a long annealing time (3713 min), shown in Fig. 12, clearly exhibited a speckled pattern, some grains may have become very large even in the intermediate layer. There would be growth competition between the grains in the intermediate layer and those in the oriented layers growing in the thickness direction. For a comparatively thick specimen, the time required for the total invasion of the intermediate layer is substantially longer, which would allow the grains to grow even in the intermediate layer. In case of grains in the intermediate layer that had already grown quite large, it is not possible for the oriented layer to incorporate these grains because the grains are large enough to resist invasion by the oriented layers. This is also a possible explanation for the change in the grain growth mode (spontaneous slowing down) in the thickness direction.

Acknowledgements This study was partially supported by a Grant-in-Aid for Scientific Research on Innovative Areas “New Polymeric Materials Based on Element-Blocks” (No. 15H00742) from the Ministry of Education, Culture, Sports, Science, and Technology of Japan. The SAXS experiments were performed under the approval of the Photon Factory (High Energy Research Organization, Tsukuba, Japan) Program Advisory Committee (Proposal No: 2015G590). We thank Mr. Shigeo Suita for his help with the image processing.

Compliance with ethical standards

Conflict of interest The authors declare no conflict of interest.

References

- Sakurai S. Progress in control of microdomain orientation in block copolymers—efficiencies of various external fields. *Polymer*. 2008;49:2781–96.
- Ohnogi H, Sasaki S, Sakurai S. Evaluation of grain size by small-angle X-ray scattering for a block copolymer film in which cylindrical microdomains are perpendicularly oriented. *Macromol Symp*. 2016;366:35–41.
- Sakurai S, Harada T, Ohnogi H, Isshiki T, Sasaki S. Characterization of the surface morphology and grain growth near the surface of a block copolymer thin film with cylindrical microdomains oriented perpendicular to the surface. *Polym J*. 2017;49:655–63.
- Harrison C, Adamson DH, Cheng Z, Sebastian JM, Sethuraman S, Huse DA, Register RA, Chaikin PM. Mechanisms of ordering in striped patterns. *Science*. 2000;290:1558–60.
- Ji S, Liu C, Liao W, Fenske AL, Craig GSW, Nealey PF. Domain orientation and grain coarsening in cylinder-forming poly(styrene-*b*-methyl methacrylate) films. *Macromolecules*. 2011;44:4291–300.
- Black CT, Guarini KW. Structural evolution of cylindrical-phase diblock copolymer thin films. *J Polym Sci*. 2004;42:1970–5.
- Hu X, Zhu Y, Gido SP, Russell TP, Iatrou H, Hadjichristidis N, Abuzaina FM, Garetz BA. The effect of molecular architecture on the grain growth kinetics of A_nB_n star block copolymers. *Faraday Discuss*. 2005;128:103–12.
- Harrison C, Angelescu DE, Trawick M, Cheng Z, Huse DA, Chaikin PM, Vega DA, Sebastian JM, Register RA, Adamson DH. Pattern coarsening in a 2D hexagonal system. *Europhys Lett*. 2004;67:800–6.
- Vega DA, Harrison CK, Angelescu DE, Trawick ML, Huse DA, Chaikin PM, Register RA. Ordering mechanisms in two-dimensional sphere-forming block copolymers. *Phys Rev E*. 2005;71:061803.
- Honda K, Sasaki S, Sakurai S. Spontaneous orientation of the body-centered-cubic lattice for spherical microdomains in a block copolymer thin film. *Kobunshi Ronbunshu*. 2017;74:75–84.
- Kim JK, Lee HH, Sakurai S, Aida S, Masamoto J, Nomura S, Kitagawa Y, Suda Y. Lattice disordering and domain dissolution transitions in polystyrene-*block*-poly(ethylene-*co*-but-1-ene)-*block*-polystyrene triblock copolymer having a highly asymmetric composition. *Macromolecules*. 1999;32:6707–17.
- Shimizu N, Mori T, Igarashi N, Ohta H, Nagatani Y, Kosuge T, Ito K. Refurbishing of small-angle X-ray scattering beamline, BL-6A at the photon factory. *J Phys*. 2013;425:202008.
- Dosch H, Batterman BW, Wack DC. Depth-controlled grazing-incidence diffraction of synchrotron X radiation. *Phys Rev Lett*. 1986;56:1144–7.
- Bayomi RAH, Aoki T, Shimojima T, Takagi H, Shimizu N, Igarashi N, Sasaki S, Sakurai S. Structural analyses of sphere- and cylinder-forming triblock copolymer thin films near the free surface by atomic force microscopy, X-ray photoelectron spectroscopy, and grazing-incidence small-angle X-ray scattering. *Polymer*. 2018;147:202–212.
- Tomita S, Urakawa H, Wataoka I, Sasaki S, Sakurai S. Complete and comprehensive orientation of cylindrical microdomains in a block copolymer sheet. *Polym J*. 2016;48:1123–31.
- Rasband W. ImageJ, U.S. National Institutes of Health, Bethesda, Maryland, USA. <https://imagej.nih.gov/ij/>.
- Ohnogi H, Isshiki T, Sasaki S, Sakurai S. Intriguing transmission electron microscopy images observed for perpendicularly oriented cylindrical microdomains of block copolymers. *Nanoscale*. 2014;6:10817–23.
- Stein GE, Cochran EW, Katsov K, Fredrickson GH, Kramer EJ, Li X, Wang J. Symmetry breaking of in-plane order in confined copolymer mesophases. *Phys Rev Lett*. 2007;98:158302.
- Stein GE, Kramer EJ, Li X, Wang J. Layering transitions in thin films of spherical-domain block copolymers. *Macromolecules*. 2007;40:2453–60.
- Sakurai S, Momii T, Taie K, Shibayama M, Nomura S, Hashimoto T. Morphology transition from cylindrical to lamellar microdomains of block copolymers. *Macromolecules*. 1993;26:486–91.
- Siggia ED. Late stages of spinodal decomposition in binary mixtures. *Phys Rev A*. 1979;20:595–605.
- Nojima S, Tsutsumi K, Nose T. Phase separation process in polymer systems. I. Light scattering studies on a polystyrene and poly(methylphenylsiloxane) mixture. *Polym J*. 1982;14:225–32.
- Nojima S, Ohyama Y, Yamaguchi M, Nose T. Phase separation process in polymer systems. III. spinodal decomposition in the critical mixture of polystyrene and poly(methylphenylsiloxane) and scaling analysis. *Polym J*. 1982;14:907–12.
- Domb C, Lebowitz, JL, editors. Phase transition and critical phenomena. London: Academic Press; 1983.

25. Utracki LA, Verlag CH, editors. Current topics in polymer science. Munich: Hanser; 1987. pp. 199–242.
26. Hashimoto T, Itakura M, Shimidzu N. Late stage spinodal decomposition of a binary polymer mixture. II. Scaling analyses on $Q_m(\tau)$ and $I_m(\tau)$. *J Chem Phys.* 1986;85: 6773–86.
27. Nose T. Kinetics of phase separation in polymer mixtures. *Phase Transit.* 1987;8:245–60.
28. Hashimoto T. Dynamics in spinodal decomposition of polymer mixtures. *Phase Transit.* 1988;12:47–119.
29. Araki T, Tran-Cong Q, Shibayama M, editors. Structure and properties of multiphase polymeric materials. New York: Marcel Dekker; 1998. p. 35.
30. Onuki, A. Phase transition dynamics. Cambridge: Cambridge University Press; 2002.
31. Nambu T, Yamauchi Y, Kushiuro T, Sakurai S. Micro-convection, dissipative structure and pattern formation in polymer blend solutions under temperature gradients. *Faraday Discuss.* 2005; 128:285–98.
32. Watanabe H, Sato T, Osaki K. Concentration dependence of loop fraction in styrene-isoprene-styrene triblock copolymer solutions and corresponding changes in equilibrium elasticity. *Macromolecules.* 2000;33:2545–50.
33. Yokoyama H, Mates TE, Kramer EJ. Structure of asymmetric diblock copolymers in thin films. *Macromolecules.* 2000;33: 1888–98.